# Electronic Supplementary Information

## Two-dimensional computational method for generating planar electrode patterns with enhanced volumetric electric fields and its application to continuous dielectrophoretic bacterial capture

Chang-Ho Han[a], Hyun Wook Ha[b], Jaesung Jang[a, c, †]

[a] School of Mechanical, Aerospace and Nuclear Engineering, Ulsan National Institute of Science and Technology (UNIST), Ulsan 44919, Republic of Korea

[b] Daegu Gyeongbuk Institute of Science and Technology, Daegu 42988, Republic of Korea

[c] Department of Biomedical Engineering, UNIST, Ulsan 44919, Republic of Korea

[†]Correspondence should be addressed to jjang@unist.ac.kr; Tel: +82-52-217-2323; Fax: +82-52-217-2449

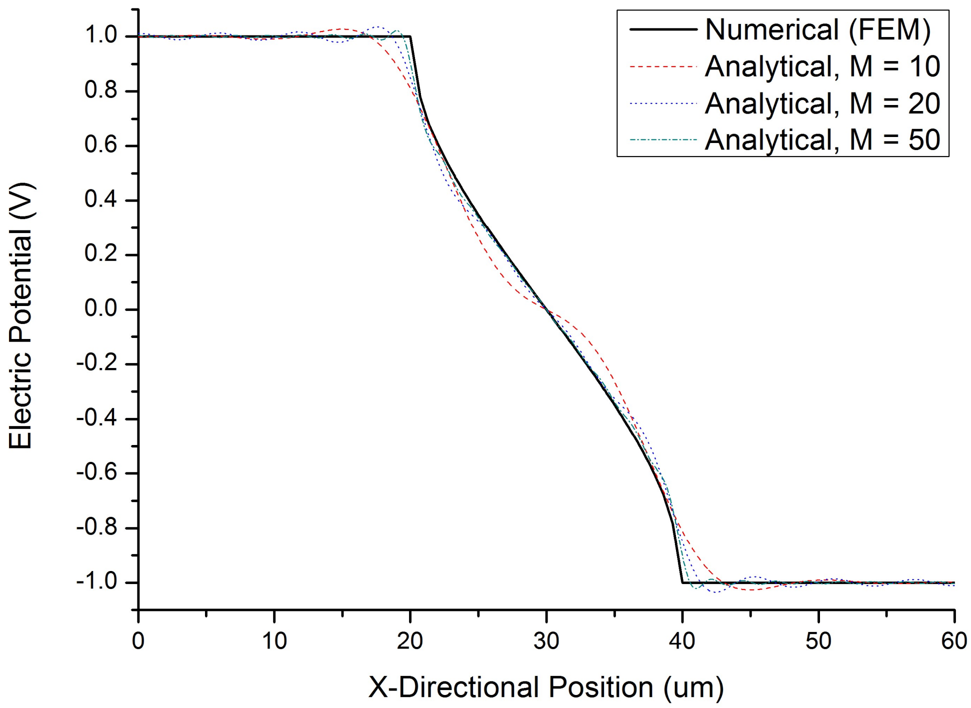


**Figure S-1.** Numerically and analytically calculated electric potential distributions of Fig. 2a at $\boldsymbol{z} = \mathbf{0}$ ($\boldsymbol{V_0}$ = 1 V, $\boldsymbol{d}$ = 20 μm), where the analytic electric potential was $\boldsymbol{\varphi(x, z = 0)} = \sum_{m=0}^{\infty} \boldsymbol{G_m \cos\frac{m\pi x}{a} \cosh\left(-\frac{m\pi}{a}h\right)}$ under the truncated number of $\boldsymbol{m}$ from 0 to $\boldsymbol{M}$ [1].

**Table S-1.** Calculated $\boldsymbol{G_m}$ with $\boldsymbol{m}$ for Fig. 2a and Fig. S-1 ($\boldsymbol{V_0}$ = 1 V, $\boldsymbol{d}$ = 20 μm).

| $\boldsymbol{m}$ | $\boldsymbol{G_m}$ | **12** | -1.02E-21 | **25** | 1.44E-12 | **38** | 5.82E-30 |
|---|---|---|---|---|---|---|---|
| **0** | 5.92E-17 | **13** | 2.85E-07 | **26** | -6.35E-27 | **39** | -7.48E-19 |
| **1** | 0.801729 | **14** | 2.30E-21 | **27** | -1.04E-13 | **40** | 1.22E-30 |
| **2** | -6.37E-18 | **15** | -2.14E-08 | **28** | -8.94E-28 | **41** | -1.17E-19 |
| **3** | -0.02298 | **16** | -8.75E-23 | **29** | -1.32E-14 | **42** | -3.84E-32 |
| **4** | 2.52E-17 | **17** | -1.88E-09 | **30** | 2.38E-28 | **43** | 3.25E-20 |
| **5** | -0.00055 | **18** | -5.78E-24 | **31** | 3.81E-15 | **44** | 5.51E-33 |
| **6** | -3.31E-18 | **19** | 5.92E-10 | **32** | 1.26E-28 | **45** | -2.25E-21 |
| **7** | 0.000196 | **20** | 2.32E-24 | **33** | -2.69E-16 | **46** | 3.26E-33 |
| **8** | 5.70E-19 | **21** | -4.39E-11 | **34** | 1.12E-28 | **47** | -3.89E-22 |
| **9** | -1.38E-05 | **22** | 8.33E-25 | **35** | -3.83E-17 | **48** | 7.37E-34 |
| **10** | -1.08E-20 | **23** | -4.78E-12 | **36** | 9.01E-29 | **49** | 1.16E-22 |
| **11** | -8.58E-07 | **24** | 3.83E-27 | **37** | 1.08E-17 | **50** | 2.59E-35 |

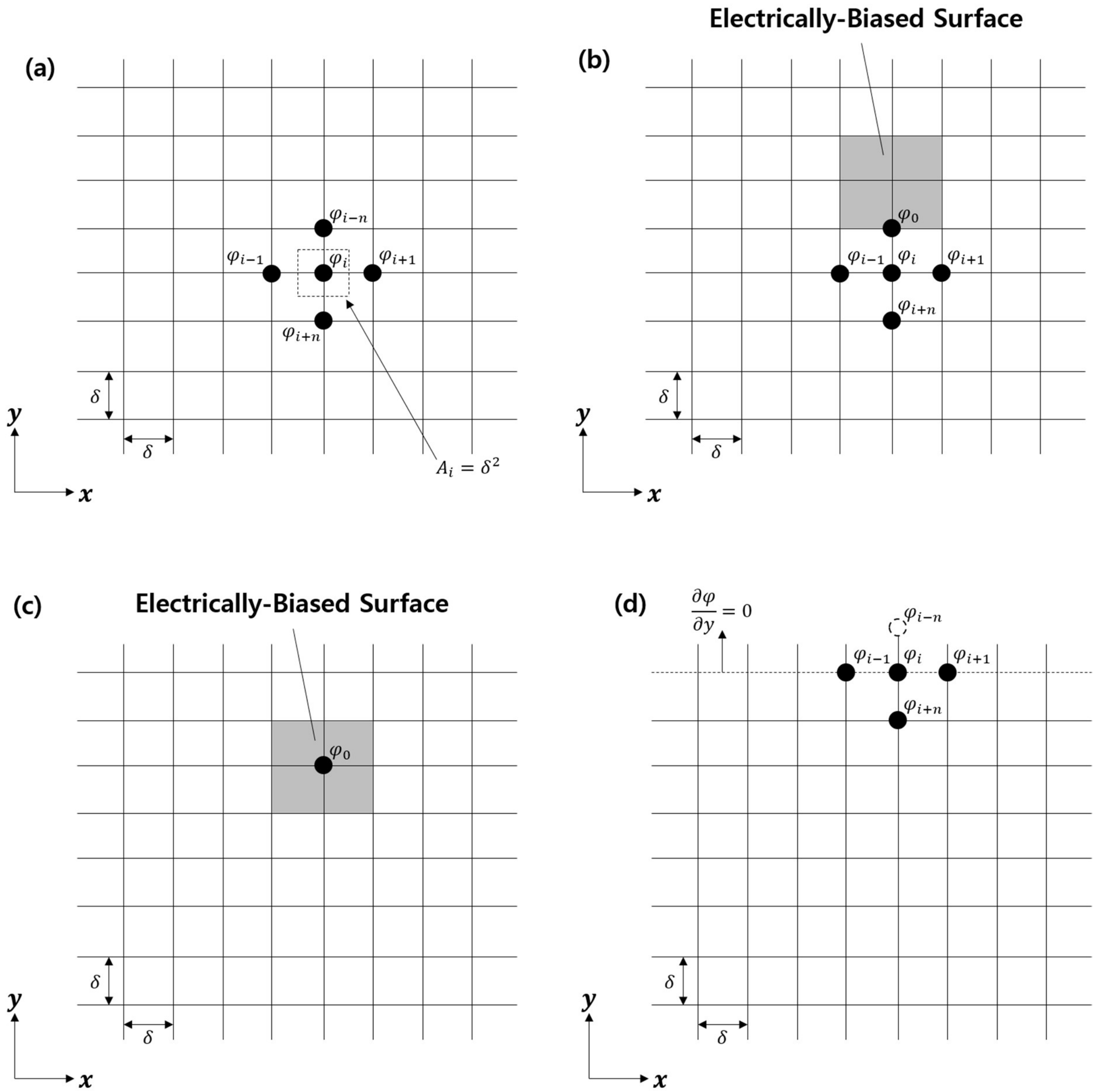


**Figure S-2.** Finite difference equations for electric potential on a planar electrode can be derived for several representative cases: **(a)** The electric potential $\boldsymbol{\varphi_i}$ is equal to the average of the electric potentials of the four neighboring points, **(b)** One of the neighboring points is on the boundary of the electrically-biased surface, **(c)** The electric potential $\boldsymbol{\varphi_i}$ is inside the electrically-biased surface, and **(d)** Some of the neighboring points are on the electrically insulated boundaries.

**Derivation of Finite Difference Equations for Electric Potential on a 2D Plane**

Laplace equation for the electrical potential on a 2D plane can be shown as

$$\frac{\partial^2 \varphi}{\partial x^2} + \frac{\partial^2 \varphi}{\partial y^2} = 0. \tag{S-1}$$

According to the second-order central difference scheme, the second order partial derivatives can be approximated as (Fig. S-2a)

$$\left.\frac{\partial^2 \varphi}{\partial x^2}\right|_i = \frac{\varphi_{i-1}+\varphi_{i+1}-2\varphi_i}{\delta^2}, \text{ and} \tag{S-2}$$

$$\left.\frac{\partial^2 \varphi}{\partial y^2}\right|_i = \frac{\varphi_{i-n}+\varphi_{i+n}-2\varphi_i}{\delta^2}, \tag{S-3}$$

where $i$ is a grid index, $\varphi_i$ is the electric potential at grid $i$, $\delta$ is the distance between the neighboring grids, and $n$ is the number of grid columns. The resulting Laplace equation can be given by

$$\varphi_{i-n} + \varphi_{i-1} - 4\varphi_i + \varphi_{i+1} + \varphi_{i+n} = 0. \tag{S-4}$$

If one of the neighboring grids has a fixed electric potential as shown in Fig. S-2b, where $\varphi_{i-n} = \varphi_0$ is a fixed electric potential, Eq. S-4 is shown as

$$\varphi_{i-1} - 4\varphi_i + \varphi_{i+1} + \varphi_{i+n} = -\varphi_0. \tag{S-5}$$

If grid $i$ and the neighboring grids are biased to the same fixed electric potential, the electric potential at the grid $i$ is simply $\varphi_i = \varphi_0$ (Fig. S-2c). When the grid $i$ is on an electrically insulated surface, $\varphi_{i-n} = \varphi_{i+n}$ (Fig. S-2d) and Eq. S-4 is given by

$$\varphi_{i-1} - 4\varphi_i + \varphi_{i+1} + 2\varphi_{i+n} = 0. \tag{S-6}$$

Finite difference equations for electric potentials at all grid points can be obtained in the same manner and solved using MATLAB.

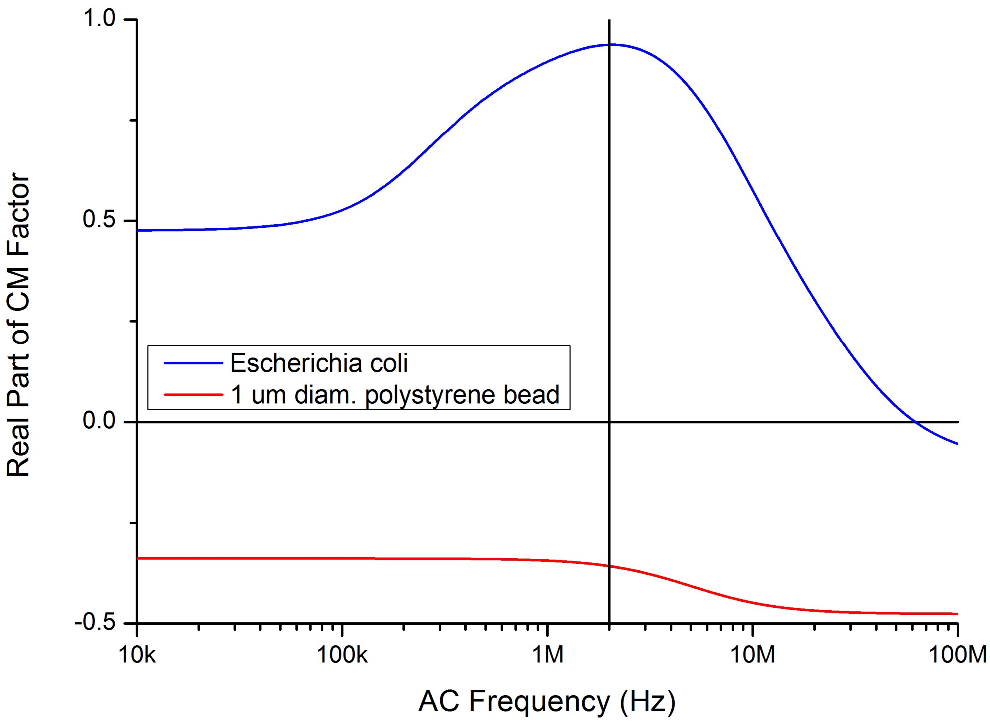


**Figure S-3.** Real parts of the Clausius-Mossotti (CM) factors for *E. coli* and 1-µm-diameter polystyrene beads, suspended in 0.01× PBS buffer (199 µS/cm) [2–4].

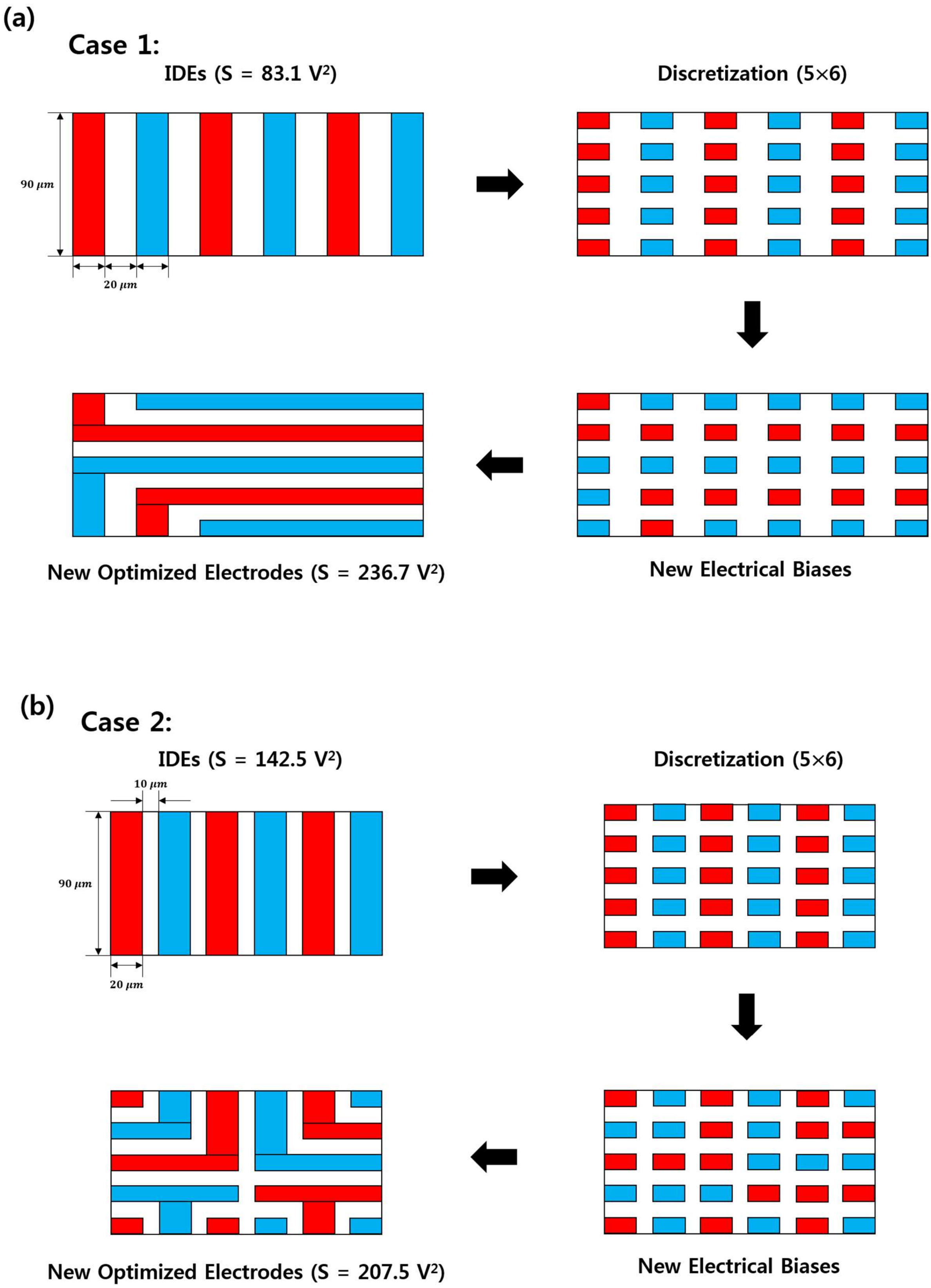


**Figure S-4.** MED process for 6 lines of IDEs. **(a)** case 1. **(b)** case 2.

**3D Multiphysics Simulation using COMSOL**

3D simulation was conducted using a commercial software COMSOL Multiphysics® 4.3. A 720 μm long (x-), 90 μm wide (y-), and 18 μm high (z-) microchannel with different electrode patterns on the bottom surface was designed. Flow and electrostatics modules were used, and the obtained flow fields and electric potential distributions were used in the particle tracing module.

For steady incompressible laminar flow calculation, the governing equations were $\underline{\nabla} \cdot \overline{u} = 0$ and $\rho(\overline{u} \cdot \underline{\nabla})\overline{u} = \underline{\nabla} \cdot \left[-pI + \mu\left(\underline{\nabla}\overline{u} + \left(\underline{\nabla}\overline{u}\right)^{\mathrm{T}}\right)\right]$, where $\overline{u}$ is the flow velocity vector, $p$ is static pressure, $\rho$ is the density, and $\mu$ is the dynamic viscosity of a fluid. Fully-developed velocity inflow and zero pressure were set at the inlet and outlet, respectively, and the other walls were set to no-slip boundary conditions ($\overline{u} = 0$). Newton-Raphson algorithms were employed to solve the nonlinear static finite element problems, with an iterative solver being the generalized minimum residual method for the linear systems having non-symmetric matrices in each step, and hence $\overline{u}$ and $p$ fields were obtained along the volumetric domain.

Laplace equation, $\nabla^2\varphi = 0$, was solved to find the electric field potentials, and as for the boundary conditions, external electrical sinusoidal signals were biased to the planar electrodes with 180° out of phases (red and blue electrodes from the MED process), and for the quasi-static electric field, the root-mean-squared (rms) electric potential is expressed as,

$$V_{rms} = \sqrt{\frac{1}{T}\int_{t_0}^{t_0+T}\left(\frac{V_{pp}}{2}\sin\omega t - \frac{V_{pp}}{2}\sin(\omega t + \pi)\right)^2 dt}, \qquad \text{(S-7)}$$

where $V_{rms}$ is the rms-valued electric potential, $T$ is the period of the sinusoidal signal, $t_0$ is an arbitrary time, $V_{pp}$ is the peak-to-peak electric potential of the signal, $\omega$ is the angular frequency of the signal, and $t$ is the time. All boundaries except for the electrodes were applied by zero charge (Neumann boundary conditions), and $V_{rms}/2$ and $-V_{rms}/2$ were given on the red and blue electrodes, respectively (Dirichlet boundary conditions) [5, 6].

Conjugate gradient method was used as an iterative solver to solve the linear static finite element problems having symmetric matrices for the $\varphi$ along the entire domain. Electric field vector fields were obtained by $\overline{E} = -\underline{\nabla}\varphi$.

Particle tracing was conducted for the bacteria using the Newtonian force model,

$$m_p \frac{d^2\overline{x}_p}{dt^2} = \overline{F}_{drag} + \overline{F}_{gravity} + \overline{F}_{buoyancy} + \overline{F}_{DEP} = -3\pi\mu d_p \left(\frac{d\overline{x}_p}{dt} - \overline{u}\right) + m_p \frac{\rho_p - \rho}{\rho_p}\overline{g} + \frac{\pi}{4} {d_p}^3 \varepsilon_m Re(K) \underline{\nabla} \left|\overline{E}\right|^2, \quad \text{(S-8)}$$

where $m_p$ is the particle mass, $\overline{x}_p$ is the position vector of the particle, $d_p$ is the particle diameter, $\rho_p$ is the particle density, $\overline{g}$ is the gravity vector, $\varepsilon_m$ is the electrical permittivity of media, $Re(K)$ is the real part of the CM factor. Here, the bacteria were assumed to be 1-μm-diameter spheres, with $\rho_p$ of 1160 kg/m$^3$ [7] and $Re(K)$ of 0.93666 (Fig. S-3). The predetermined $\overline{u}$ and $\overline{E}$ were used for the particle tracing, and a transient implicit solver generalized alpha was used with automatically chosen time steps. A total of 352 (44×8) particles were equally distributed at the inlet, and their trajectories were analyzed (Fig. 7).

To verify the solution convergence, mesh sizes were varied, and the velocity profile, $\left|\partial\left|\overline{E}\right|^2/\partial z\right|$, and final z-directional positions were checked for flow, electrostatics, and particles tracing, respectively. Also, the element order (4, 10, 20, 35 nodes per each tetrahedral element for 1st, 2nd, 3rd, and 4th order elements, respectively) was tested for flow and electrostatic simulations, and time step was controlled to acquire converged particle trajectories. The determined numerical conditions for the converged solutions were listed in Table S-2.

**Table S-2.** Numerical conditions for the converged solutions.

| | **Laminar Flow** | **Electrostatics** | **Particle Tracing** |
|---|---|---|---|
| **Tetrahedral Mesh Element Number** | 104,812 | 1,332,327 | 4,738,566 |
| **Element Order** | 2nd (velocity), 1st (pressure) | 4th (electric potential) | |

| | | | |
|---|---|---|---|
| **Time Step** | - | - | 6.13e-7 to 1 s |
| **Solving Time** | 2 min 37 sec | 20 min 28 sec | 11 hr 39 min 50 sec |
| **RAM Usage** | 3.35 GB | 39.46 GB | 15.89 GB |

**Table S-3.** **S** values for various electrodes

| **Electrode Pattern** | **Factor S** | **Fig. 2e** | **Electrode Pattern** | **Factor S** | **Figs. 4-7** |
|---|---|---|---|---|---|
| 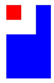 | 9.6 | ① | 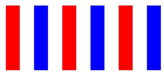 | 83.1 | IDEs (6-line; case 1) |
| 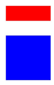 | 10.5 | ② | 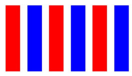 | 142.5 | IDEs (6-line; case 2) |
| 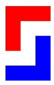 | 14.8 | ③ | 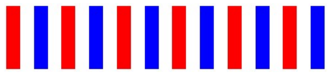 | 182.9 | IDEs (12-line; case 1) |
| 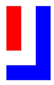 | 15.6 | ④ | 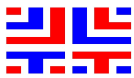 | 207.5 | MED-optimized Electrodes (from 6-line IDEs; case 2) |
| 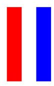 | 16.5 | ⑤ | 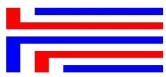 | 236.7 | MED-optimized Electrodes (from 6-line IDEs; case 1) |
| 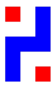 | 19.2 | ⑥ | 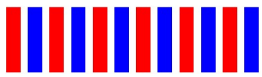 | 313.5 | IDEs (12-line; case 2) |
| 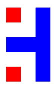 | 19.2 | ⑦ | 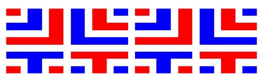 | 437.5 | MED Electrodes (from 12-line IDEs; case 2) |
| 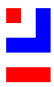 | 20.1 | ⑧ | 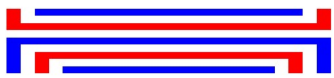 | 491.5 | MED Electrodes (from 12-line IDEs; case 1) |
| 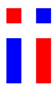 | 24.0 | ⑨ | | | |

## 2D Simulation using COMSOL for Six IDEs

We conducted 2D simulations on six IDEs having 20 μm widths and different gaps ranging from 1 to 15 μm in a 90 μm high microfluidic channel using Comsol. The flow rates changed from 40 to 40000 nl/min, and -1V and +1V were applied to the electrodes. The number of captured particles increased with the electrode gap for lower flow rates and decreased for higher flow rates. This is because the low electric field intensity in the larger gaps may be sufficient for particle capture because of low flow rates. Also, larger gap IDEs have larger working areas, which means that electric field is applied over large areas, and hence the particles under the electric field may have a higher probability to be captured on the electrodes.

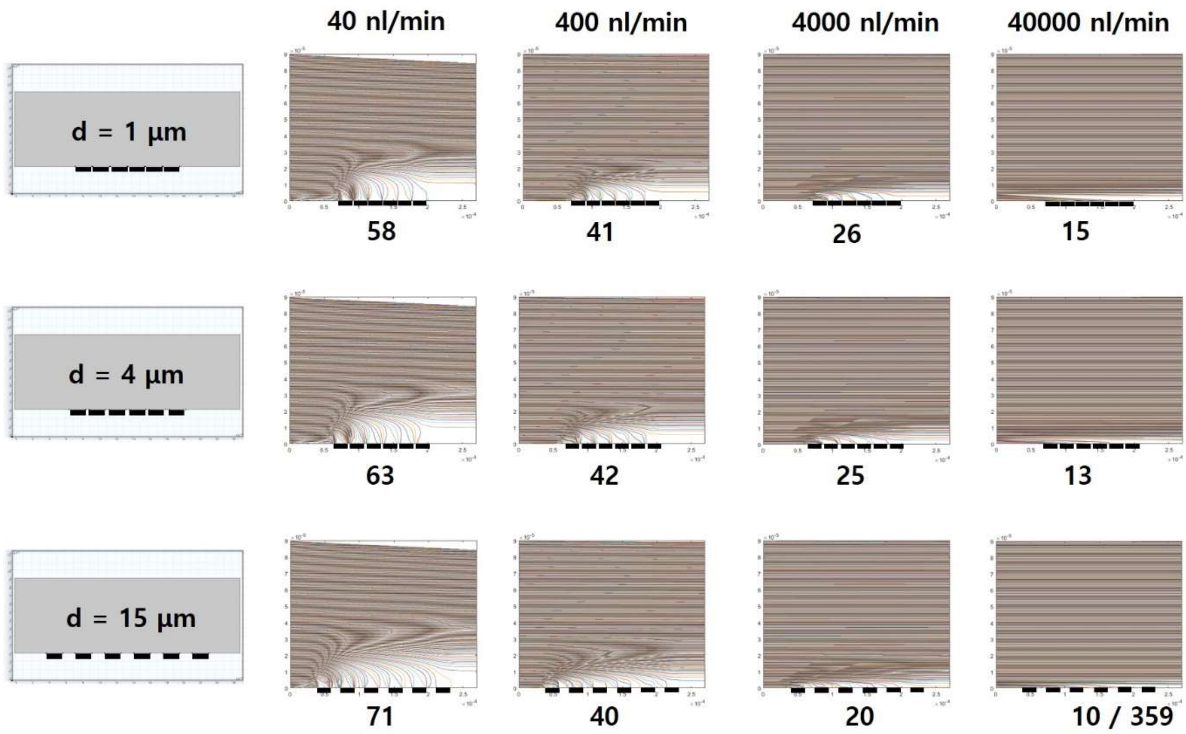


**Figure S-5.** The particle tracks for different electrode gaps and flow rates.

Therefore, we also plotted the number of captured particles based on the number density (the number of captured particles/working areas), and the particle capture density decreased with the electrode gap for all flow rates, as shown below. Interestingly, the electrode with 3 μm gap has higher values of **S** and **S**/working area, but had lower particle capture density than the electrode with 4 μm gap for 40 nl/min (the lowest flow rate case) although the particle capture density increased with the increasing values of **S** and **S**/working area for other flow rates. Even for the lowest flow rate case, the general trend shows that the particle capture density increased with the increasing values of **S** and **S**/working area.

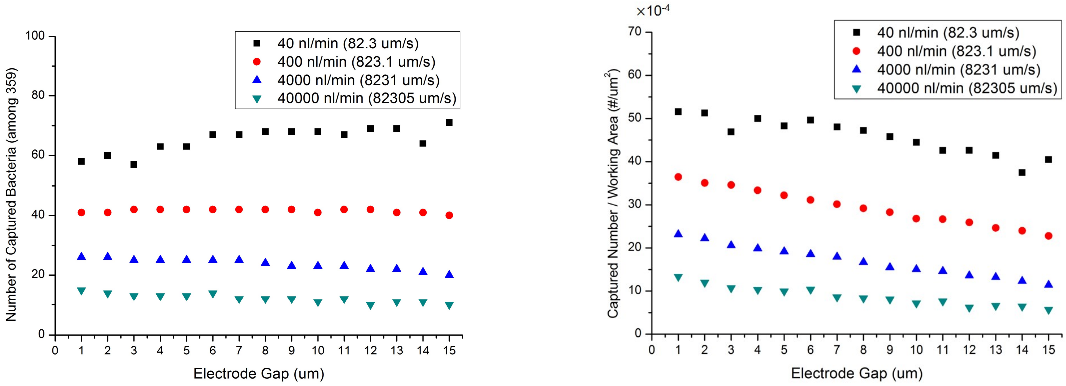


**Figure S-6.** The number of captured particles (left) and the particle capture density (right) for different electrode gaps and flow rates, where the values of **S** and **S**/working area decreased with the increasing electrode gap.

## References

[1] H. Song and D. J. Bennett, *J. Fluids Eng.*, 2008, **130**, 081605.

[2] K. Asami, T. Hanai, N. Koizumi, *Biophys. J.*, 1980, **31**, 215-228.

[3] S. Park, Y. Zhang, T. -H. Wang, S. Yang, *Lab Chip*, 2011, **11**, 2893.

[4] C.-H. Han, S. Y. Woo, J. Bhardwaj, A. Sharma and J. Jang, *Sci. Rep.*, 2018, **8**, 14942.

[5] N. G. Green, A. Ramos, A. Gonzalez, A. Castellanos, H. Morgan, *J. Electrostat.*, 2001, **54**, 71-87.

[6] J. Oh, R. Hart, J. Capurro, H. Noh, *Lab Chip*, 2009, **9**, 62-78.

[7] M. Godin, A. K. Bryan and T. P. Burg, *Appl. Phys. Lett.*, 2007, **91**, 123121.